Chemical Science

ROYAL SOCIETY OF CHEMISTRY

EDGE ARTICLE

Cite this: *Chem. Sci.*, 2024, **15**, 3661

All publication charges for this article have been paid for by the Royal Society of Chemistry

Designing dynamic coordination bonds in polar hybrid crystals for a high-temperature ferroelastic transition†

Yao-Bin Li,[a] Xiao-Xian Chen,[a] Wei-Jian Xu,[b] Ya-Ping Gong,[a] Hui Ye,[a] Zhi-Shuo Wang[a] and Wei-Xiong Zhang *[a]

Received 13th December 2023
Accepted 29th January 2024

DOI: 10.1039/d3sc06702e

rsc.li/chemical-science

Ferroelastic materials have gained widespread attention as promising candidates for mechanical switches, shape memory, and information processing. Their phase-transition mechanisms usually originate from conventional order–disorder and/or displacive types, while those involving dynamic coordination bonds are still scarce. Herein, based on a strategic molecular design of organic cations, we report three new polar hybrid crystals with a generic formula of AA′RbBiCl$_6$ (A = A′ = Me_3SO^+ for **1**; A = Me_3SO^+ and A′ = Me_4N^+ for **2**; A = A′ = $Me_3NNH_2^+$ for **3**). Their A-site cations link to the $[RbBiCl_6]_n^{2n-}$ inorganic framework with **lon** topology through Rb–O/N coordination bonds, while their significantly different interactions between A′-site cations and inorganic frameworks provide distinct phase-transition behaviour. In detail, the strongly coordinative A′-site Me_3SO^+ cations prevent **1** from a structural phase transition, while coordinatively free A′-site Me_4N^+ cations trigger a conventional order–disorder ferroelastic transition at 247 K in **2**, accompanied by a latent heat of 0.63 J g^{-1} and a usual "high → low" second-harmonic-generation (SHG) switch. Interestingly, the A′-site $Me_3NNH_2^+$ cations in **3** reveal unusual dynamic coordination bonds, driving a high-temperature ferroelastic transition at 369 K with a large latent heat of 18.34 J g^{-1} and an unusual "low → high" SHG-switching behaviour. This work provides an effective molecular assembly strategy to establish dynamic coordination bonds in a new type of host–guest model and opens an avenue for designing advanced ferroelastic multifunctional materials.

Introduction

Ferroelastics, crucial ferroic materials known for their stress–strain behaviour, play a pivotal role in various applications, including mechanical switches, shape memory, and actuator.[1–5] Among them, research on organic-inorganic hybrid crystals exhibiting ferroelastic phase transitions has thrived over the past decade, benefiting from their structural diversity, eco-friendly synthesis, and mechanical flexibility.[6–15] Currently, the majority of documented ferroelastic phase transitions in hybrid crystals can be classified as mechanisms involving order–disorder and/or displacive type mechanisms.[16–27] For instance, (homopiperazine-1,4-diium)[K(BF_4)$_3$] exhibits a ferroelastic phase transition above room temperature, which is attributed to synergic order–disorder transitions of organic cations and BF_4^- bridges.[19] Besides, an unconventional type of structural phase transition, termed the bond-switching phase transition, has gained significant attention.[28–31] Unlike order–disorder and displacive ones, bond-switching phase transitions, characterized by reversible generation/cleavage of coordination bonds, induce dramatic changes in the crystal structure crossing different crystal systems, thereby facilitating the triggering of ferroelastic transitions.[32,33] Understanding the mechanism behind such unconventional bond switching is essential for the design of novel ferroic materials. However, the relevant research is in its infant stages, as there are very few examples of hybrid crystals with dynamic (switchable or changeable) coordination bonds.

We previously reported two cyanide-bridged hybrid crystals, (Me_3NOH)[KFe(CN)$_6$] and (Me_3NNH_2)$_2$[Co(CN)$_6$Na(H_2O)], both of which show bond-switching transitions.[28,33] We noticed that the switchable coordination bonds should be highly associated with delicate host–guest interactions, which are significantly related to the selection of the host–guest model, metal ions, and organic cations with coordination groups. In this context, besides the few known examples of bond-switching transitions in cyanide-bridged hybrid systems, it is a prerequisite to broaden the scope of host–guest systems for comprehensively understanding and exploring bond-switching transitions.

[a]*MOE Key Laboratory of Bioinorganic and Synthetic Chemistry, School of Chemistry, IGCME, Sun Yat-Sen University, Guangzhou 510275, China. E-mail: zhangwx6@mail.sysu.edu.cn*

[b]*Department of Chemistry, CICECO-Aveiro Institute of Materials, University of Aveiro, 3810-193 Aveiro, Portugal*

† Electronic supplementary information (ESI) available. CCDC 2313516–2313519 and 2313598. For ESI and crystallographic data in CIF or other electronic format see DOI: https://doi.org/10.1039/d3sc06702e

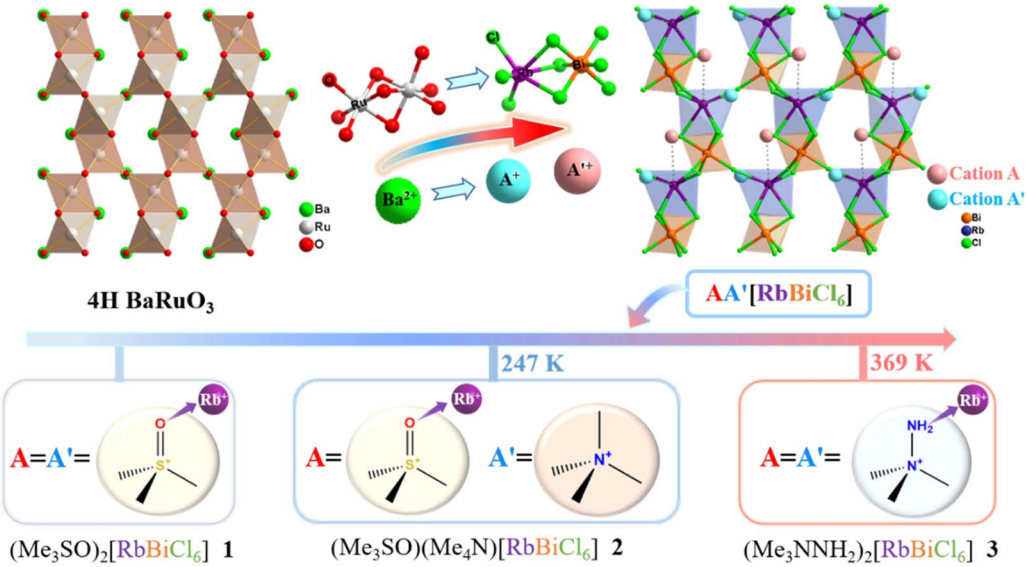

Scheme 1 Three new polar hybrid crystals obtained by modifying the 4H $BaRuO_3$ structure and a strategic molecular design of organic cations, which adopt a generic formula of AA′[$RbBiCl_6$], exhibiting different phase-transition behaviours due to different coordination interactions of A′-site organic cations.

Recently, our attention was captivated by some bimetal halides with non-perovskite structures,[34–36] such as (*R*-3-hydroxypyrrolidinium)$_2$RbBiBr$_6$ and (3-hydroxypyrrolidinium)$_2$-RbBiBr$_6$.[34,35] They share the same formula of $A_2BB'X_6$, where A is an organic cations, X is a halogen anion, and B and B′ are trivalent and monovalent metal cations, respectively, and adopt a non-perovskite three-dimensional (3D) structure consisting of a $[BB'X_6]_n^{2n-}$ inorganic framework with a fascinating 4-connected **lon** topology created through alternating connected face- and corner-sharing Rb/Bi-centred polyhedra, resembling the 4H $BaRuO_3$ structure.[37,38] From a microscopic perspective, the interaction of the organic components with an inorganic framework through Rb–O coordination bonds provides a significant clue for designing bond-switching transitions. However, it is likely due to their larger size that the employed cyclic organic cations (such as *R*-3-hydroxypyrrolidinium and 3-hydroxypyrrolidinium) are hard to rotate in the relatively smaller pores but are strongly connected to the inorganic framework with coordination bonds, and thus their structural phase-transition mechanisms are not involved in dynamic coordination bonds.

Herein, we introduce some globular organic cations with coordination capacity to design new hybrid crystals based on the strategy of coordinate unit-transmutation from a 4H $BaRuO_3$ structure and demonstrate how to achieve an unconventional transition with dynamic coordination bonds. Three new hybrid crystals with a formula of AA′$RbBiCl_6$ (A = A′ = Me_3SO^+ for **1**; A = Me_3SO^+ and A′ = Me_4N^+ for **2**; A = A′ = $Me_3NNH_2^+$ for **3**) were successfully synthesized, in which all A-site cations coordinatively link to Rb^+ ions whereas the different coordination interactions of A′-site cations endow **1–3** with distinct phase-transition behaviours (Scheme 1). In detail, **1** remains phase stable as its A′-site Me_3SO^+ cations form strong Rb–O coordination bonds. **2** undergoes a phase transition at 247 K, mainly induced by the order–disorder transition of coordinatively free A′-site Me_4N^+ cations, suggesting that smaller-sized organic cations that are reasonably substituted drive the dynamics changes of the coordination bond. By contrast, **3** undergoes a phase transition with a large latent heat at 369 K as its A′-site $Me_3NNH_2^+$ cations reveal unusual dynamic coordination bonds, *i.e.*, changing from a coordinative and order state at a room-temperature phase to a much weaker coordinative and disorder state at a high-temperature phase. Detailed structural phase-transition analyses were conducted by using thermal methods, dielectric measurements, and variable-temperature single-crystal structures, highlighting the role of organic cations in promoting bond-switching transitions. Noteworthily, **2** and **3** exhibit distinct heat-driven second-harmonic-generation (SHG) behaviour due to vastly different changes of coordination interactions, *i.e.* a usual "high → low" SHG-switching behaviour in **2** and an unusual "low → high" SHG-switching behaviour in **3**.

Experimental

Materials and syntheses

All chemicals were commercially available and used without further purification. The crystals of the three compounds were prepared by the slow evaporation of the hydrochloric acid solutions of RbCl, $BiCl_3$, and corresponding organic ammonium salts in a stoichiometric ratio. The yield was 82% for **1**, 75% for **2** and 72% for **3**, respectively, based on $BiCl_3$. The purities of samples were verified using powder X-ray diffraction (PXRD) patterns (Fig. S1–S3†).

Instrumentation

PXRD patterns were obtained using a Bruker D8 ADVANCE X-ray powder diffractometer (Cu Kα, λ = 1.54184 Å). Using 5 mg powder samples, thermogravimetric analysis (TGA) was carried out on a TG 209 F3 Tarsus system with a heating rate of 10

K min^{-1} under a nitrogen atmosphere. Differential scanning calorimetry (DSC) measurements were performed on a TA DSC Q2000 instrument by using 8 mg powder samples. Using powder-pressed samples (plate samples with an area of 113 mm^2 and a thickness of 0.3 mm), the temperature-dependent dielectric measurement was performed on a TH2838 impedance analyser at frequencies from 10 kHz to 1 MHz, with an applied voltage of 1.0 V. The SHG signal was measured using an XPL1064-200 instrument at a heating/cooling rate of 5 K min^{-1}. The observation of ferroelastic domains was performed by using an OLYMPUS BX41 polarizing microscope at a heating/cooling rate of 3 K min^{-1}.

Single-crystal X-ray diffraction data were collected on a SuperNova single-crystal diffractometer by using Mo Ka (λ = 0.71073 Å) radiation. Absorption corrections were applied by using the multi-scan program CrysAlisPro. All structures were solved by direct methods and refined by the full-matrix least-squares technique with the SHELX program package on Olex^2.[39,40] Anisotropic thermal parameters were applied to all non-hydrogen atoms. The hydrogen atoms were generated geometrically. Detailed crystallographic data and structural refinement parameters are listed in Tables S1 and S2.†

Results and discussion

Thermal analyses

Thermogravimetric analysis indicated that the three compounds exhibit thermal stability up to 490 K (**1**), 510 K (**2**), and 540 K (**3**), respectively. DSC measurements were conducted to analyze the phase transition behaviours. As shown in Fig. 1, the DSC curves for **1** do not exhibit any endothermic or exothermic peaks, indicating the absence of a structural phase transition within the measured temperature range. In contrast, distinct heat anomalies were observed during heating and cooling processes for **2** and **3**. In detail, we observed a pair of endothermic/exothermic peaks at 247/245 K during the heating/cooling runs for **2**, indicating a reversible phase transition, while **3** exhibited a pair of prominent thermal anomalies at 369/364 K, revealing an above-room-temperature phase transition.

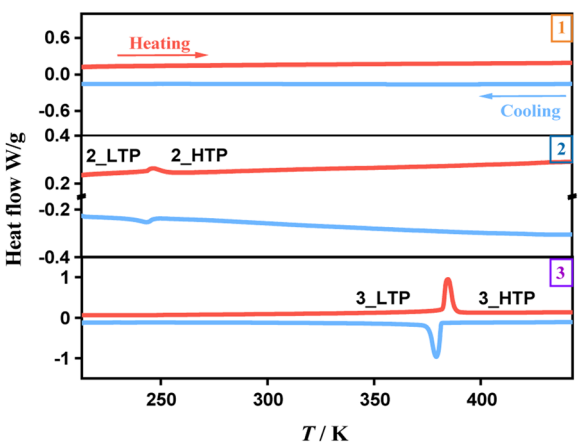

Fig. 1 DSC curves in a heating–cooling run for **1**, **2**, and **3**.

The total latent heat values of **2** and **3** in the heating process are estimated to be 0.63 and 18.34 J g^{-1}, respectively. Accordingly, their total entropy changes (ΔS) in the heating process are estimated to be 1.71 and 32.68 J mol^{-1} K^{-1}, respectively. In comparison, **3** reveals a greater thermal stability, a higher phase-transition temperature, a larger latent heat, and a larger entropy change than **2**, implying relatively dramatic changes during the phase transition in **3**. For convenience, the phases above phase-transition temperature are labeled as the high-temperature phases (HTPs) and the phases below phase-transition temperature as the low-temperature phases (LTPs).

Crystal structures

The crystal structures of the three compounds were determined by using variable-temperature single-crystal X-ray diffraction to investigate their phase transition mechanisms. **1** adopts a 3D structure formed by ordered Me_3SO^+ cations and an $[RbBiCl_6]_n^{2n-}$ anionic framework with a polar space group of $P112_1$ at 210 K. As shown in Fig. 2a, each Bi^{3+} ion is surrounded by six Cl^- ions to form a $BiCl_6$ octahedron, while each Rb^+ ion is located in a distinct $RbCl_6O_2$ dodecahedron and coordinated by six Cl^- ions and two axially occupied O atoms from two organic cations, namely, the guest cations link to the host inorganic skeleton by Rb–O coordination bonds. Notably, the structure of **1** is distinctive to conventional 3D hybrid double perovskites, such as $(CH_3NH_3)_2KGdCl_6$ and $(CH_3NH_3)_2AgBiBr_6$, where both metal halogen octahedra are interconnected through corner-sharing mode.[41,42] It features a unique 3D network where the $BiCl_6$ octahedron and $RbCl_6O_2$ dodecahedron are alternately linked through a combination of corner-sharing and face-sharing. Such a 3D inorganic framework can be described as a 4-connected **lon** topology with a Schlafli symbol of 6^6, in which both the Rb and Bi centres are the 6^6 nodes. Furthermore, the inorganic $BiCl_6$ octahedron exhibits a slightly distorted configuration, as evidenced by the unequal Bi–Cl lengths (Table S3†). The $RbCl_6O_2$ dodecahedron shows more pronounced distortion due to the presence of Rb–O coordination bonds. Specifically, the Rb–O coordination bond lengths (2.782 and 2.995 Å) are significantly shorter than the Rb–Cl bond lengths (ranging from 3.346–3.448 Å).

The crystal structure of the 2_LTP closely resembles that of **1**, adopting a 3D **lon** topology structure and crystallizing in monoclinic space group $P112_1$. As shown in Fig. 2c, each Bi^{3+} ion forms coordination with six Cl^- ions, creating a $BiCl_6$ octahedron. Each Rb^+ ion connects with six Cl^- ions and one Me_3SO^+ ion, while Me_4N^+ cations occupy the void of the 3D inorganic framework formed by the alternately connected $BiCl_6$ octahedron and $RbCl_6O$ decahedron. Likewise, the collective arrangement of the organic components and inorganic framework results in polarity along the *c* axis.

Upon heating to above 247 K (2_HTP), the crystal structure transformed into hexagonal space group $P6_3$. As shown in Fig. 2d, Me_3SO^+ cations have slight swing while Me_4N^+ cations become highly disordered as they can freely rotate in the voids of the 3D framework. Consequently, the phase transition mechanism of **2** can be classified as an order–disorder type.

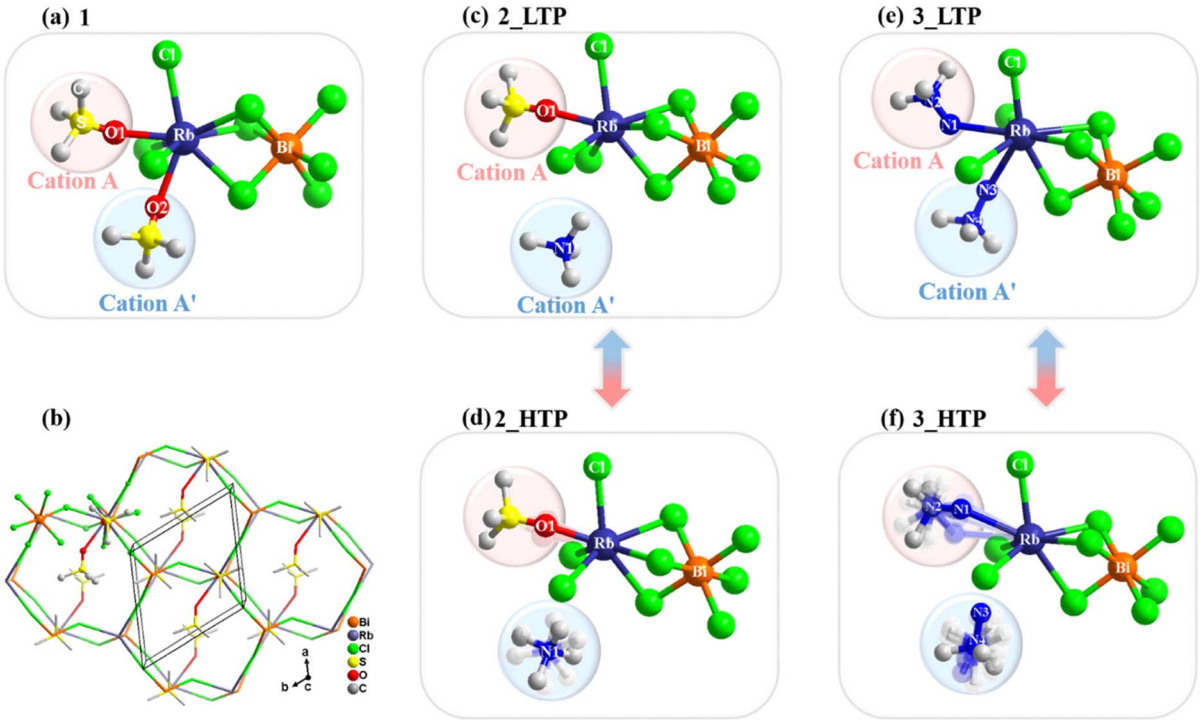

Fig. 2 The basic unit of the framework in **1** (a), 2_LTP (c), 2_HTP (d), 3_LTP (e), and 3_HTP (f). (b) Perspective view of the packing structure along the *c*-axis of **1**. H atoms of the organic cations were omitted for clarity.

During the phase transition from $P6_3$ to $P112_1$, the number of symmetry operations decreased from 6 (E, $2C_6$, $2C_3$, and C_2) to 2 (E and C_2), indicating that **2** belongs to a ferroelastic transition (6*F*2) according to Aizu.[43]

Similarly, the 3_LTP features a 3D $[RbBiCl_6]_n^{2n-}$ anionic inorganic framework with **lon** topology and well-ordered organic cations. As shown in Fig. 2e, each Bi^{3+} coordinates with six Cl^- ions, with Bi–Cl bond lengths ranging from 2.685–2.736 Å. The Rb^+ ion exhibits a dual coordination environment, involving six Cl^- ions (Rb–Cl bond lengths of 3.258–3.524 Å) and two axially occupied $-NH_2$ groups from two $Me_3NNH_2^+$ cations. Both weak Rb–N coordination interactions (3.217–3.570 Å) and N–H···Cl hydrogen bonds lead to an orthorhombic $Pna2_1$ space group for the 3_LTP, distinguishing between **1** and **2**. The pronounced structural distortion in the $RbCl_6N_2$ dodecahedron of **3**, akin to that observed in the $RbCl_6O_2$ polyhedron in **1**, primarily arises from the unequal bond lengths in the Rb–Cl and Rb–N bonds.

Upon heating, the structure transforms from the orthorhombic $Pna2_1$ phase (3_LTP) into polar hexagonal space group $P6_3mc$ (3_HTP). In the 3_HTP, both $Me_3NNH_2^+$ organic cations become 6-fold disordered, while half of them no longer remain connected to Rb^+ ions through Rb–N coordination interactions. Meanwhile, the $BiCl_6$ octahedron shows a more pronounced distortion than that in the 3_LTP (Bi–Cl bond lengths, 2.681–2.721 Å). Therefore, it is reasonable to conclude that during the transition from the 3_LTP to the 3_HTP, the dynamical motions of organic cations drive the Rb–N coordination bonds to experience a bond-switching behaviour from a bonded state to a broken state. Such a unique phase-transition mechanism stands in stark contrast to the mechanisms observed in previously reported metal halides. Moreover, such bond-switching behaviour in **3** leads to a larger entropy change compared to that in **2**, which could provide a significant clue for exploration of barocaloric materials.[33,44] The space group changes from $P6_3mc$ in the 3_HTP (with symmetric elements: E, $2C_6$, $2C_3$, C_2, $3\sigma_v$, and $3\sigma_d$) to $Pna2_1$ in the 3_LTP (with symmetric elements: E, C_2, and $2\sigma_v$), following the symmetry breaking principle with an Aizu notation 6*mmFmm*2, indicating a possible ferroelastic transition.

Temperature-dependent SHG signal and dielectric responses

The structural phase transitions in **2** and **3** were further verified by variable-temperature SHG and dielectric measurements. Fig. 3a and c depict the temperature-dependent SHG signal of powder samples for **2** and **3**, showing their SHG-activating nature in all phases, consistent with non-centrosymmetric structures as revealed by single-crystal X-ray diffraction. The transition temperatures of the SHG signal are coincident with the corresponding peak temperatures observed in DSC curves, testifying their structural phase transitions. For **2**, a noticeable SHG signal (0.42 times of potassium dihydrogen phosphate, KDP) was observed at the 2_LTP, and gradually decreased to 0.12 times of KDP for the 2_HTP, exhibiting a common "high → low" SHG-switching behaviour. In contrast, for **3**, the SHG signal at the 3_LTP was about 0.22 times of KDP and increased to 0.46 times of KDP at the 3_HTP, exhibiting an unusual "low → high" SHG-switching behaviour. This phenomenon differs from most of the

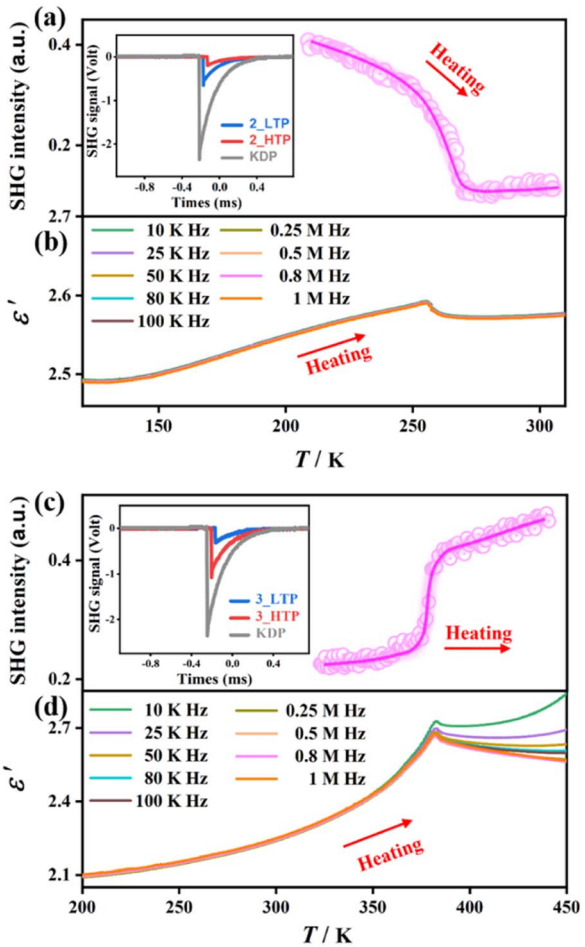

Fig. 3 Temperature-dependent SHG intensity and the real part of complex dielectric permittivity for **2** (a) and (b) and **3** (c) and (d).

known SHG switches, which reveal an "on → off" or "high → low" SHG switch upon heating,[45–47] such as $NH_4[(CH_3)_4N]SO_4 \cdot H_2O$ and $[(R)$-3-hydroxy-pyrrolidinium$]_5Sb_4Br_{17}$.

The different SHG behaviours between **2** and **3** indicate a direct correlation between the observed SHG variations and their unique structural changes, particularly related to the distortion of inorganic octahedra and the order–disorder transition of organic cations. To understand structure–property relationship, we quantitatively estimated the distortion of the octahedra (Δd) using the following equation:

$$\Delta d = \left(\frac{1}{6}\right) \sum \left[\frac{d_n - d}{d}\right]^2$$

where d_n is the individual Bi–Cl bond length and d refers to the average length of the Bi–Cl in the $BiCl_6$ octahedron.[48,49] The Δd of the $BiCl_6$ octahedron in the 2_LTP was calculated to be 8.51×10^{-5}, verifying that the $BiCl_6$ octahedron is distorted with Bi atoms deviating from their ideal positions. Upon heating above 247 K (2_HTP), the Δd of the $BiCl_6$ octahedron reduced to 3.27×10^{-5} and all coordinatively free A′-site cations (Me_4N^+) became highly disordered, hence leading to a usual "high → low" SHG-switching behaviour for **2**. By contrast, **3** undergoes a drastic structural phase transition accompanied by changeable Rb–N coordination interactions, resulting in a pronounced distortion of the $BiCl_6$ octahedron (Δd increases from 3.07×10^{-5} in the 3_LTP to 6.04×10^{-5} in the 3_HTP). Such a pronounced distorted octahedron, together with 6-fold disordered A-site cations ($Me_3NNH_2^+$) that coordinate with Rb^+ ions, contribute to the observed unusual "low → high" SHG-switching behaviour for **3**.

The variable-temperature dielectric constants were measured on the pressed polycrystalline samples for **2** and **3**. Upon heating, as illustrated in Fig. 3b and d, prominent dielectric anomalies are observed near the phase-transition temperature, consistent with the results of DSC measurement. Such dielectric anomalies recur during both the heating and cooling processes, demonstrating the reversible nature of phase transitions. Specifically, upon heating, **2** exhibits a slight dielectric anomaly, with the real part of dielectric constants (ε') at a frequency of 1 MHz varying from 2.49 at 120 K to 2.57 at 290 K. In contrast, **3** exhibits relatively noticeable dielectric anomalies around the phase-transition temperature, with the ε' value varying from 2.1 at 200 K to 2.6 at 440 K. The distinct dielectric responses should be attributed to the order–disorder transition of the non-polar Me_4N^+ cation in **2** and the polar $Me_3NNH_2^+$ cation in **3**.[50]

Temperature-dependent lattice parameters

The temperature-dependent lattice parameters were obtained *via* Pawley refinements on the variable-temperature PXRD patterns in the temperature range of 193–303 K for **2** and 333–413 K for **3** (Tables S6 and S7†), and the thermal expansion coefficients were calculated using the PASCal program (Table S10†).[51] The volume expansion coefficient decreases from $+240 \times 10^{-6}$ K^{-1} in the 2_LTP to $+140 \times 10^{-6}$ K^{-1} in the 2_HTP and decreases from $+260 \times 10^{-6}$ K^{-1} in the 3_LTP to $+185 \times 10^{-6}$ K^{-1} in the 3_HTP. As shown in Fig. 4a, upon heating, an increase of the crystallographic axes by 0.13–0.97% and a slight increase in cell volume by *ca.* 0.39% at 245 K were observed during the transition from the 2_LTP to the 2_HTP. In contrast, during the transition from the 3_LTP to the 3_HTP at 369 K, a significant decrease in the *a*-axis length by 2.49% was observed. Meanwhile, a substantial increase was observed in the *b*-axis lengths by 3.08%, while an increase in *c*-axis lengths by 0.63% and a slight increase in cell volume by 1.15% were detected. Such large changes on the *a*-axis and *b*-axis lengths in **3** are in accord with the larger entropy changes and dielectric anomalies arising from the dynamic coordination bonds.

Ferroelastic phase transitions and spontaneous strains

To further verify the ferroelastic phase transition for **2** and **3**, the evolution of domains on an as-grown single crystal was inspected by thermal stimulus in polarization microscopy (Fig. S12 and S13†). As shown in Fig. 5a, no observable domain structures appeared at the 2_HTP (the paraelastic phase). As the sample cooled to 240 K (the ferroelastic phase), the complex but fuzzy domains emerged, which faded away upon reheating to the paraelastic phase. Moreover, using the cell parameters at 245 K

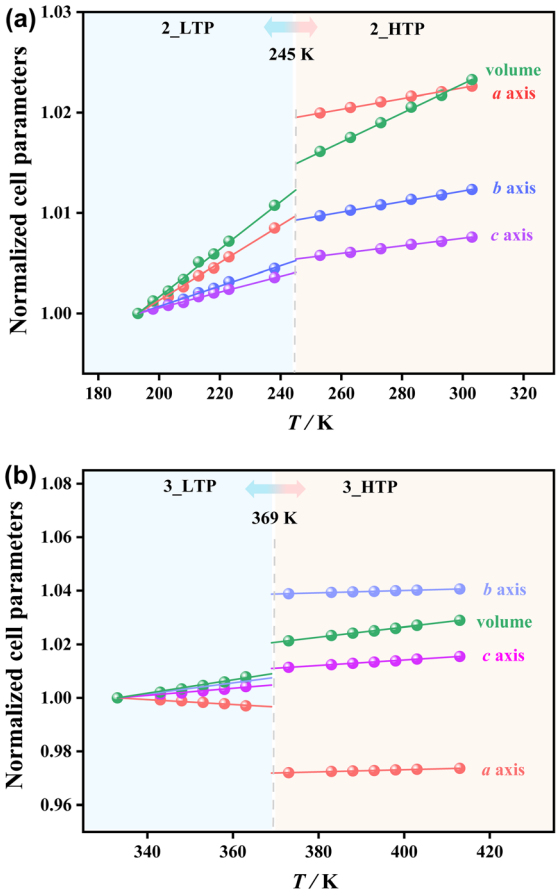

Fig. 4 Temperature-dependent normalized cell parameters for **2** (a) and **3** (b).

deduced by linear fitting variable-temperature cell parameters (Table S8†), the total spontaneous strain of 0.0167 was estimated for **2**, and the fuzzy ferroelastic domains might be ascribed to the small spontaneous strain. As mentioned above in structure analysis, **3** exhibits a one-step ferroelastic transition with an Aizu notation of 6*mmFmm*2 accompanied by a total spontaneous strain of 0.0399 from the cell parameters at 369 K deduced by linear fitting variable-temperature cell parameters (Table S9†). These spontaneous strain values are among the intermediate levels in the reported hybrid ferroelastics.[6–15] It should be emphasized that the greater spontaneous strain in **3** compared to **2** is closely associated with more drastic structural changes. As shown in Fig. 5b, a multi-domain structure was absent at the 3_LTP, with the mono-domain state remaining persistent through the 3_HTP. Upon cooling the sample to 360 K (the ferroelastic phase), evident striped domains emerged, disappearing when heated back to 375 K.

Hirshfeld surface analyses

These three compounds share a similar host inorganic framework but differ in their guest organic cations, implying that their distinct phase-transition behaviours primarily stem from varying host–guest intermolecular interactions. Therefore, a comprehensive investigation into the intermolecular interactions among the three compounds was performed by Hirshfeld surface analyses.[52] The surfaces are depicted using a colour scheme of red, white, and blue indicating the shorter contacts, the van der Waals separation, and longer contacts, respectively. As shown in Fig. 6a, d and g, the red areas of the surfaces for guest cations originate from the H···Cl and O/N···Rb contacts in **1**, **2**, and **3**, respectively, revealing that the predominant host–guest interactions between the inorganic skeleton and organic cations are hydrogen bonding interactions and Rb–O/N coordination bonds. Among them, A-site cations always coordinatively link to Rb^+ ions whereas the A′-site cations adopt different coordination modes; thus A-site cations from the three compounds exhibit the same host–guest interactions, while their A′-site cations show markedly different host–guest interactions. In decomposed fingerprint plots (Fig. 6c, f and i), approximately 3.3%, 0%, and 1.9% of the Hirshfeld surface area of A′-site cations were associated with Rb–O/N coordination bonds in **1**, **2**, and **3**, respectively. Meanwhile, the smallest (d_i, d_e) pairs from A′-site cations indicated that the strongest O/N···Rb short contacts are (1.36 Å, 1.64 Å) for **1** and (1.61 Å, 1.91 Å) for **3**. Specifically, the interactions associated with the Rb–O coordination bond in **1** appear to be stronger than that of the Rb–N coordination bond in **3**. This observation suggests that the Rb–O coordination bond formed by Me_3SO^+ cations is more resilient and less prone to breakage compared to the Rb–N coordination bond from $Me_3NNH_2^+$ cations. Consequently, **1** does not undergo a bond-switching phase transition before its decomposition, whereas **3** undergoes an above-room-temperature

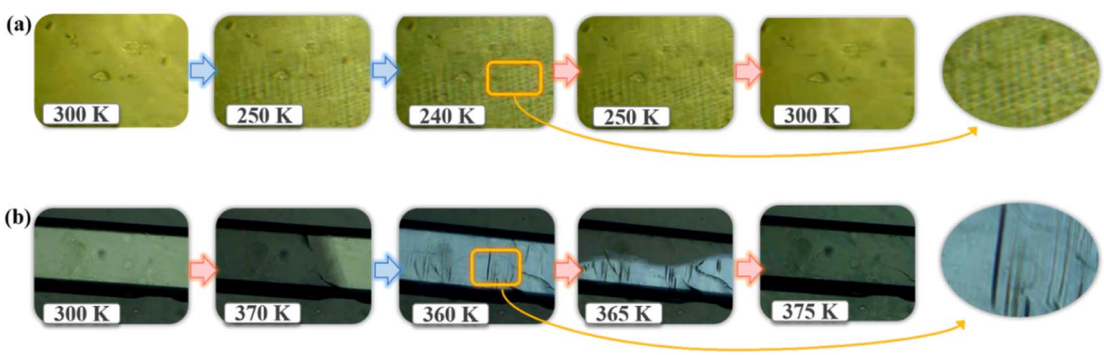

Fig. 5 Polarized microscopy observations at different temperatures for **2** (a) and **3** (b).

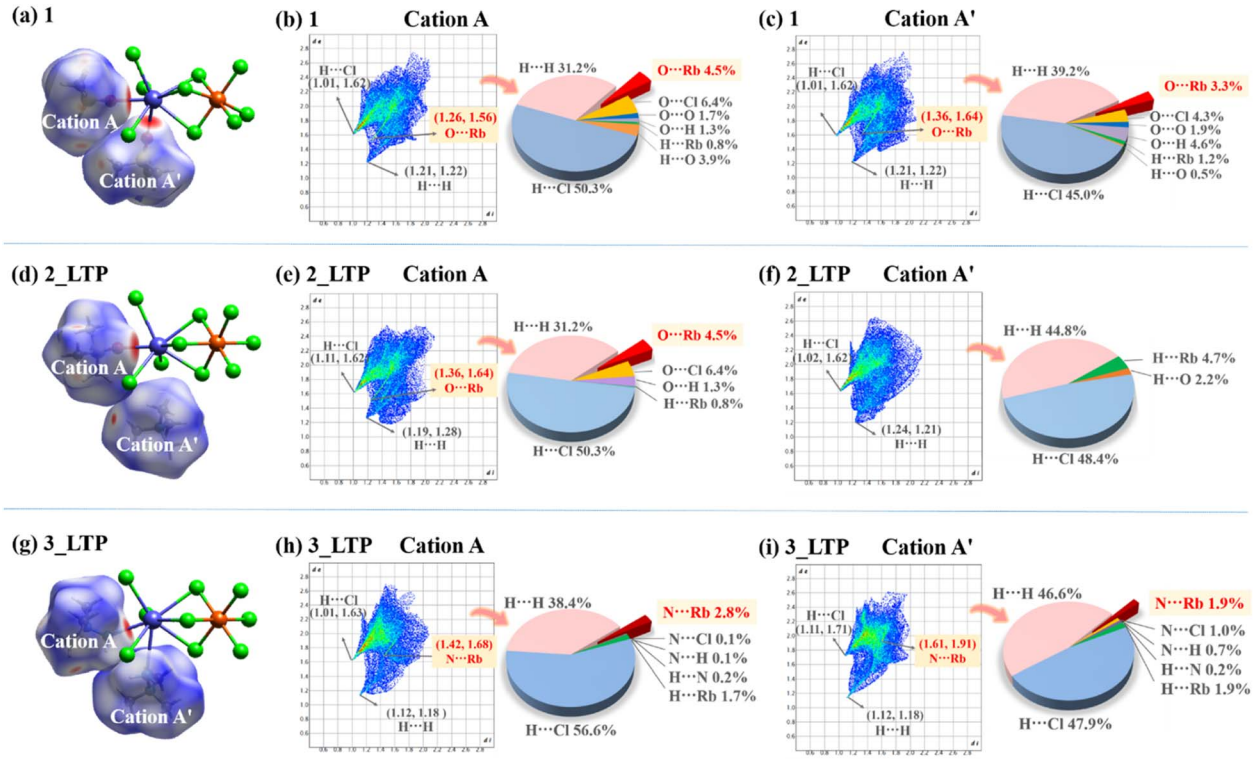

Fig. 6 The Hirshfeld surfaces of **1** (a), 2_LTP (d), and 3_LTP (g). The fingerprint plots of guest cations for **1** (b) and (c), 2_LTP (e) and (f), and 3_LTP (h) and (i).

phase transition due to the changeable/dynamic Rb–N coordination bonds.

For **2**, coordinatively free A′-site Me_4N^+ cations primarily engaged in weak C–H···Cl host–guest interactions and H···H guest–guest interactions, enabling it to readily undergo an order–disorder phase transition at a relatively low temperature of 247 K. In contrast, strong guest–guest interactions are observed in **3**, evidenced by the smallest H···H short contact (1.12 Å, 1.18 Å) and the largest Hirshfeld surface area of H···H short contact. As a result, the intensified repulsive interactions among the adjacent guest cations, together with the Rb–N coordination interactions from A′-site cations in **3**, lead to a ferroelastic transition occurring at above room temperature.

In short, it is reasonable to deduce that the subtle changes in guest molecules influence the host–guest and guest–guest interactions, fostering competitive yet balanced intermolecular dynamics. These modifications enable the creation of multiple inter-convertible crystalline states, governed by specific activation energy barriers, thus leading to distinct phase-transition behaviours. This understanding is crucial for designing and comprehending unique structural phase transitions, particularly bond-switching transitions.

Conclusions

In summary, we demonstrated a strategic molecular design of organic cations in a new kind of host–guest model with an **lon** topologic inorganic framework, by presenting three new polar hybrid crystals, *i.e.*, **1–3**, with a generic formula of $AA'RbBiCl_6$. Their A-site cations link to Rb^+ ions *via* strong Rb–O/N coordination bonds, while their A′-site cations reveal significantly different interactions that drive distinct phase-transition behaviours. A′-site Me_3SO^+ cations form strong Rb–O coordination bonds, preventing **1** from triggering a structural phase transition, whereas coordinatively free A′-site Me_4N^+ cations induce an order–disorder ferroelastic transition at 247 K and a usual heating-induced "high → low" SHG switch in **2**. Remarkably, A′-site $Me_3NNH_2^+$ cations form unusual dynamic coordination bonds in **3**, driving a high-temperature ferroelastic phase transition accompanied by the larger entropy change and an unusual heating-induced "low → high" SHG switch. Such systematic investigations into phase transitions not only deepen the understanding of exceptional bond-switching transitions but also hold significant promise for guiding the development of functional hybrid materials.

Author contributions

WX Zhang and YB Li conceived the idea, designed the experiments, and co-wrote the manuscript. YB Li performed the synthesis experiments, DSC, dielectric, SHG, crystal structural analysis, ferroelastic domain observations, and the Hirshfeld surface analyses. XX Chen and WJ Xu assisted in crystal structural analyses. YP Gong and H Ye assisted in the Pawley refinements. ZS Wang offered advice on experimental design.

Conflicts of interest

There are no conflicts to declare.

Acknowledgements

This work was supported by the NSFC (22071273 and 21821003), Fundamental Research Funds for the Central Universities (Sun Yat-Sen University, 23lgzy001).

Notes and references

1 Y. Hu, L. You, B. Xu, T. Li, S. A. Morris, Y. Li, Y. Zhang, X. Wang, P. S. Lee and H. J. Fan, *Nat. Mater.*, 2021, **20**, 612–617.
2 E. K. Salje, *Annu. Rev. Mater. Res.*, 2012, **42**, 265–283.
3 M. Liu, B. M. Howe, L. Grazulis, K. Mahalingam, T. Nan, N. X. Sun and G. J. Brown, *Adv. Mater.*, 2013, **25**, 4886–4892.
4 S. Baek, H. Jang, C. Folkman, Y. Li, B. Winchester, J. Zhang, Q. He, Y. Chu, C. Nelson and M. Rzchowski, *Nat. Mater.*, 2010, **9**, 309–314.
5 Y. Zhang, M.-G. Han, J. A. Garlow, Y. Tan, F. Xue, L.-Q. Chen, P. Munroe, N. Valanoor and Y. Zhu, *Nano Lett.*, 2019, **19**, 5319–5326.
6 E. Strelcov, Q. Dong, T. Li, J. Chae, Y. Shao, Y. Deng, A. Gruverman, J. Huang and A. Centrone, *Sci. Adv.*, 2017, **3**, e1602165.
7 B.-Q. Zhao, X.-X. Chen, H. Ye, Y.-P. Gong, J. Wang, L. Ye and W.-X. Zhang, *Chem. Sci.*, 2023, **14**, 5965–5973.
8 R. G. Xiong, S. Q. Lu, Z. X. Zhang, H. Cheng, P. F. Li and W. Q. Liao, *Angew. Chem., Int. Ed.*, 2020, **132**, 9661–9665.
9 M. M. Lun, C. Y. Su, J. Li, Q. Q. Jia, H. F. Lu, D. W. Fu, Y. Zhang and Z. X. Zhang, *Small*, 2023, **19**, 2303127.
10 Z. Yue, F. Wu, X. Li, Y. Liu, J. Luo and X. Liu, *Sci. China Mater.*, 2023, **66**, 3977–3983.
11 Q. Liu, H. Peng, J.-C. Qi, Y.-Z. Lu, S.-J. Yang and W.-Q. Liao, *Chem. Commun.*, 2023, **59**, 1793–1796.
12 D.-X. Liu, Z.-H. Yu, X.-X. Chen, W.-X. Zhang and X.-M. Chen, *Chin. Chem. Lett.*, 2023, **34**, 107310.
13 Y.-P. Gong, X.-X. Chen, G.-Z. Huang, W.-X. Zhang and X.-M. Chen, *J. Mater. Chem. C*, 2022, **10**, 5482–5488.
14 X.-X. Chen, D.-X. Liu, Y.-P. Gong, S.-S. Wang, W.-X. Zhang and X.-M. Chen, *Inorg. Chem.*, 2022, **61**, 2219–2226.
15 D.-X. Liu, X.-X. Chen, Z.-M. Ye, W.-X. Zhang and X.-M. Chen, *Sci. China Mater.*, 2022, **65**, 263–267.
16 W. Luo, N. Wang, H.-K. Li, Z.-J. Xu, Y. Feng, X.-b. Fu, C. Shi, H.-Y. Ye and L.-P. Miao, *Inorg. Chem. Front.*, 2023, **10**, 5082–5088.
17 H. Ye, X.-X. Chen, D.-X. Liu, B.-Q. Zhao, Y.-B. Li, Y. Zeng, W.-X. Zhang and X.-M. Chen, *Chem. Sci.*, 2022, **13**, 14124–14131.
18 Y. Xu, K. Xu, L. He, T.-J. Yin, J. Mu, J.-T. Men, W. Zhang and Q. Ye, *Inorg. Chem.*, 2023, **62**, 1279–1285.
19 X.-X. Chen, X.-Y. Zhang, D.-X. Liu, R.-K. Huang, S.-S. Wang, L.-Q. Xiong, W.-X. Zhang and X.-M. Chen, *Chem. Sci.*, 2021, **12**, 8713–8721.
20 H. Zhang, Q.-L. Li, Y.-H. Tan, Y.-Z. Tang, X.-W. Fan, J.-L. Luo, F.-X. Wang and M.-Y. Wan, *Inorg. Chem.*, 2023, **62**, 10847–10853.
21 Q.-R. Meng, W.-J. Xu, W.-H. Hu, H. Ye, X.-X. Chen, W. Yuan, W.-X. Zhang and X.-M. Chen, *Chem. Commun.*, 2021, **57**, 6292–6295.
22 W. Yuan, Y. Zeng, Y.-Y. Tan, J.-H. Zhou, W.-J. Xu, W.-X. Zhang and X.-M. Chen, *Chem. Commun.*, 2019, **55**, 8983–8986.
23 Y. Gong, X. Chen, B. Zhao, J. Wang, W. Zhang and X. Chen, *Chin. Chem. Lett.*, 2023, **34**, 108282.
24 W.-J. Xu, P. Zelenovskii, A. Tselev, L. Verissimo, K. Romanyuk, W. Yuan, W.-X. Zhang, A. Kholkin and J. Rocha, *Chem. Commun.*, 2023, **59**, 11264–11267.
25 T. J. Yin, K. Xu, L. He, X. Meng, Y. Xu, J. T. Men, J. Mu, Q. Ye and P. P. Shi, *Chem.–Eur. J.*, 2023, **29**, e202203606.
26 G.-H. Ni, Y.-X. Sun, C.-X. Ji, Y.-W. Jin, M.-Y. Liu, J.-P. Zhao and F.-C. Liu, *Cryst. Growth Des.*, 2022, **22**, 3428–3434.
27 D. Fu, Z. Hou, Y. He, J.-C. Liu, H.-P. Lv and Y.-Y. Tang, *Chem. Mater.*, 2022, **34**, 3518–3524.
28 W.-J. Xu, P.-F. Li, Y.-Y. Tang, W.-X. Zhang, R.-G. Xiong and X.-M. Chen, *J. Am. Chem. Soc.*, 2017, **139**, 6369–6375.
29 H.-Y. Zhang, N. Zhang, Y. Zhang, H.-H. Jiang, Y.-L. Zeng, S.-Y. Tang, P.-F. Li, Y.-Y. Tang and R.-G. Xiong, *Phys. Rev. Lett.*, 2023, **130**, 176802.
30 W.-J. Xu, K. Romanyuk, Y. Zeng, A. Ushakov, V. Shur, A. Tselev, W.-X. Zhang, X.-M. Chen, A. Kholkin and J. Rocha, *J. Mater. Chem. C*, 2021, **9**, 10741–10748.
31 R. Li, T. Zhu, Z. k. Zhu, J. Wu, Y. Geng and J. Luo, *Small*, 2023, 2306825.
32 X.-G. Chen, Z.-X. Zhang, Y.-L. Zeng, S.-Y. Tang and R.-G. Xiong, *Chem. Commun.*, 2022, **58**, 3059–3062.
33 W.-J. Xu, Y. Zeng, W. Yuan, W.-X. Zhang and X.-M. Chen, *Chem. Commun.*, 2020, **56**, 10054–10057.
34 L. He, K. Xu, P.-P. Shi, Z.-B. Liu, W. Zhang and Q. Ye, *Sci. China Mater.*, 2022, **65**, 2879–2883.
35 L. He, P.-P. Shi, L. Zhou, Z.-B. Liu, W. Zhang and Q. Ye, *Chem. Mater.*, 2021, **33**, 6233–6239.
36 J. Zhou, P. Xie, C. Wang, T. Bian, J. Chen, Y. Liu, Z. Guo, C. Chen, X. Pan, M. Luo, J. Yin and L. Mao, *Angew. Chem., Int. Ed.*, 2023, **62**, e202307646.
37 H. Seung-Tae and A. W. Sleight, *J. Solid State Chem.*, 1997, **128**, 251–255.
38 C. Felser and R. Cava, *Phys. Rev. B: Condens. Matter Mater. Phys.*, 2000, **61**, 10005.
39 O. V. Dolomanov, L. J. Bourhis, R. J. Gildea, J. A. K. Howard and H. Puschmann, *J. Appl. Crystallogr.*, 2009, **42**, 339–341.
40 G. M. Sheldrick, *Acta Crystallogr., Sect. C: Struct. Chem.*, 2015, **71**, 3–8.
41 F. Wei, Z. Deng, S. Sun, F. Zhang, D. M. Evans, G. Kieslich, S. Tominaka, M. A. Carpenter, J. Zhang and P. D. Bristowe, *Chem. Mater.*, 2017, **29**, 1089–1094.
42 Z. Deng, F. Wei, F. Brivio, Y. Wu, S. Sun, P. D. Bristowe and A. K. Cheetham, *J. Phys. Chem. Lett.*, 2017, **8**, 5015–5020.
43 K. Aizu, A. Kumada and H. Yumoto, *J. Phys. Soc. Jpn.*, 1969, **27**, 511.

44 B. Li, Y. Kawakita, S. Ohira-Kawamura, T. Sugahara, H. Wang, J. Wang, Y. Chen, S. I. Kawaguchi, S. Kawaguchi, K. Ohara, K. Li, D. Yu, R. Mole, T. Hattori, T. Kikuchi, S.-I. Yano, Z. Zhang, Z. Zhang, W. Ren, S. Lin, O. Sakata, K. Nakajima and Z. Zhang, *Nature*, 2019, **567**, 506–510.
45 S. Han, L. Li, C. Ji, X. Liu, G.-E. Wang, G. Xu, Z. Sun and J. Luo, *J. Am. Chem. Soc.*, 2023, **145**, 12853–12860.
46 H.-Y. Shen, L. He, P.-P. Shi and Q. Ye, *J. Mater. Chem. C*, 2021, **9**, 4338–4343.
47 S. Liu, Z. Sun, C. Ji, L. Li, S. Zhao and J. Luo, *Chem. Commun.*, 2017, **53**, 7669–7672.
48 K. Robinson, G. Gibbs and P. Ribbe, *Science*, 1971, **172**, 567–570.
49 L. Mao, Y. Wu, C. C. Stoumpos, M. R. Wasielewski and M. G. Kanatzidis, *J. Am. Chem. Soc.*, 2017, **139**, 5210–5215.
50 W.-J. Xu, S.-L. Chen, Z.-T. Hu, R.-B. Lin, Y.-J. Su, W.-X. Zhang and X.-M. Chen, *Dalton Trans.*, 2016, **45**, 4224–4229.
51 M. J. Cliffe and A. L. Goodwin, *J. Appl. Crystallogr.*, 2012, **45**, 1321–1329.
52 M. A. Spackman and D. Jayatilaka, *CrystEngComm*, 2009, **11**, 19–32.